Aberration-free large-area stitch-free 3D nano-printing based on binary holography

DOI:
10.1364/OE.446503

Document Version
Final published version

Citation for published version (APA):
Ren, M., Lu, W., Shao, Q., Han, F., Ouyang, W., Zhang, T., Wang, C. C. L., & Chen, S. C. (2021). Aberration-free large-area stitch-free 3D nano-printing based on binary holography. *Optics Express*, *29*(26), 44250-44263. https://doi.org/10.1364/OE.446503

Published in:
Optics Express

Research Article Vol. 29, No. 26 / 20 Dec 2021 / *Optics Express* 44250

Optics EXPRESS

Aberration-free large-area stitch-free 3D nano-printing based on binary holography

MINDAN REN,[1,4] WANPING LU,[1,4] QI SHAO,[1] FEI HAN,[1] WENQI OUYANG,[1] TIANYU ZHANG,[2] CHARLIE C. L. WANG,[2] AND SHIH-CHI CHEN[1,3,*]

[1] *Department of Mechanical and Automation Engineering, The Chinese University of Hong Kong, Shatin, Hong Kong*
[2] *Department of Mechanical, Aerospace and Civil Engineering, The University of Manchester, Manchester M1 3NJ, UK*
[3] *Centre for Perceptual and Interactive Intelligence (CPII), Hong Kong Science Park, N.T., Hong Kong SAR, China*
[4] *These authors contributed equally to this work*
[*] *scchen@mae.cuhk.edu.hk*

Abstract: Direct laser writing (DLW) has been widely used in a variety of engineering and research applications. However, the fabrication of complex and robust three-dimensional (3D) structures at submicron-level resolution by DLW is still largely limited by the laser focus quality, i.e., point spread function (PSF), laser dose, precision of mechanical scanners, and printing trajectory. In this work, we present a two-photon polymerization (TPP)-based DLW system based on a digital micromirror device (DMD) and binary holography to realize aberration-free large-area stitch-free 3D printing as well as 3D random-access scanning. First, the binary holograms, which control the amplitude, phase, and position of the laser focus, are optimized by the sensorless adaptive optics algorithm to correct the distorted wavefront in the DMD work field. Next, the DMD is synchronized to a continuously moving sample stage to eliminate stitching errors, i.e., the sample positioner simultaneously moves with the scanning focus until the structure is completed. We have fabricated large-area complex 3D structures, e.g., metamaterial structures, and micro-lenses, and 2D gray level diffractive optical elements (DOEs) with better than 100 nm resolution and optimal scanning trajectories. Notably, the variation of the scanning trajectory, laser power (dose), and voxel sizes can be realized without affecting the scanning speed, i.e., 22.7 kHz, which is equivalent to the DMD pattern rate.

1. Introduction

Two-photon polymerization (TPP)-based direct laser writing (DLW) is one of the most widely used additive manufacturing technologies for fabricating complex 3D structures at submicrometer-level resolution since its introduction [1–4]. TPP is enabled by two-photon absorption (TPA), which is a highly localized nonlinear absorption process that occurs at the focal region of a femtosecond laser. Within the focal region, the liquid photoresin is polymerized to form a nanoscale building block, i.e., voxel, which has the same shape of the laser focus [5,6]; the voxel size is determined by the laser dose, i.e., laser power and exposure time [5,7]. As such, complex 3D micro-structures can be created by raster-scanning the laser focus [8]. One of the most common design of the TPP-DLW is to employ a pair of galvo-mirrors for in-plane scanning and a piezoelectric positioner for axial scanning, which prints 3D objects serially in a layer-by-layer fashion [9,10]. Notably, when the object to be printed is larger than the work volume of the optical scanner, stitching is required and often performed via a translational stage, leading to stitching errors. The stitching errors are unavoidable due to the limited precision of the sample stage and object volume shrinkage after photopolymerization, which has been a common issue for 3D printing

#446503 https://doi.org/10.1364/OE.446503
Journal © 2021 Received 21 Oct 2021; revised 6 Dec 2021; accepted 6 Dec 2021; published 17 Dec 2021

systems. Recently, our team has developed two unique TPP fabrication methods based on a digital micromirror device (DMD) with substantially improved scanning rate and random-access scanning capability [11–13]. Yet, the system still suffers from different levels of aberration within the DMD work volume as well as stitching errors.

For TPP fabrication, the reported print resolution varies significantly depending on factors including laser power, scanning rate, scanning mode, photoresins and so on [8]. Typical lateral resolution of TPP falls between 100 - 300 nm, while the axial resolution is usually 2 - 3 times worse than the lateral resolution [8,12]. Although tens of nanometers or even 8 nm [14,15] resolution have been demonstrated by precisely matching the laser power to the polymerization threshold, the uniformity and integrity of structures written at this resolution is severely compromised with extremely low writing speeds, making it impractical for general microfabrication. The application of adaptive optics (AO) methods in TPP may be a feasible solution to achieve sub-100 nm resolution with a reasonable fabrication rate, i.e., 1–10 mm/sec. AO has been widely used in astronomical telescopes and advanced microscopy to compensate the aberration induced by air turbulence, biological specimens, or intrinsic system aberration [16–19]. Previous demonstration of AO methods in TPP systems are mainly focused on correcting the refractive index variations introduced by photoresins [16], which requires the use of an additional adaptive element, e.g., deformable mirror or liquid crystal-based spatial light modulator. However, these methods can only correct the averaged aberration for the whole work space, while the aberration in the work space is typically not uniform, resulting in suboptimal fabrication results. A low-cost and localized AO method for optimizing the point spread function (PSF) over the entire work volume of the TPP fabrication system has yet to be developed.

In this work, we present a DMD-based TPP fabrication system that realizes large-area 3D printing with discrete dose control and sub-100 nm resolution via localized AO correction, i.e., optimal wavefront correction information is directly applied to different sub work fields or individual voxels without compromising the scanning speed. For large-area printing, a stitch-free process for the DMD system is developed to entirely eliminate stitching errors by synchronizing the scanning laser focus to the sample stage which moves at a constant speed. First, high-speed laser scanning at 22.7 kHz is realized by rapidly switching the binary holograms displayed on the DMD, where each hologram contains encoded laser amplitude, phase, and location. As such, 3D random-access scanning and discrete dose control are realized. With discrete dose control, laser power can be arbitrarily adjusted with fine intervals, i.e., ~0.5 µW, at the scanning rate. The AO correction is realized by superposing the wavefront correction information to the scanning holograms, where the distorted wavefront at different locations in the work field is measured and modeled by the Zernike polynomials based on sensorless AO algorithm. By combining the stitch-free method and AO correction, seamless large-area complex 3D structures, including metamaterial structures, and micro-lenses, and 2D gray level diffractive optical elements (DOEs), have been fabricated and characterized to demonstrate the efficacy of the new capabilities and resolution of our system.

2. Methods and materials

2.1. Materials and processes

Photoresists used in all the experiments are IP-Dip (Nanoscribe GmbH). The substrates used for printing are indium tin oxide (ITO) glass. Before printing, the ITO glasses are treated with 3-(Trimethoxysilyl) propyl methacrylate (1 mM in toluene) for one hour to improve the adhesion between the microstructures and substrate, followed by acetone and water rinses. After printing, the uncured photoresist is developed by propylene glycol methyl ether acetate (PGMEA) for 15 minutes, followed by a 10-minute isopropyl alcohol (IPA) rinse. All SEM images in this work are captured by JSM-7800F with an accelerating voltage of 10 eV.

2.2. Optical setup

Figure 1 presents the optical configuration of the DMD-based TPP fabrication system. The light source is a Ti:sapphire femtosecond laser (Chameleon Vision S, Coherent) with a repetition rate of 80 MHz and an average power of 2.5 W; the laser is operated at a central wavelength of 780 nm with a pulse duration of 75 fs. The laser beam first passes through lenses L1 & L2 for collimation. Next, a blazed transmission grating (G, T-1400-800-2415-94, LightSmyth) and a 2.5× beam expander (L3 & L4) are introduced to pre-compensate the angular dispersion from the DMD [12]. The DMD (DLP 4100, 0.7” XGA, Texas Instruments), which simultaneously functions as a reflective blazed grating and a programmable binary mask, is the core device to manipulate the laser beam via the displayed holograms. After the DMD, as illustrated in Fig. 2(a), a spatial filter (SF) is placed at the back focal plane of L5 to spatially select the −1st order diffraction beam, which contains the designed wavefront information. Lastly, the scanning beam propagates to the back aperture of the objective lens (CFI Plan Fluor 40× Oil, Nikon, NA = 1.3, WD = 0.24 mm) to perform TPP fabrication at the focal region. During the calibration experiments for AO wavefront correction, two-photon emissions are collected by the right detection arm, which includes a dichroic mirror (DM, ZT670rdc, Chroma), a 4-f system (L8 & L9), and a photomultiplier tube (PMT: R10699, Hamamatsu). To monitor the fabrication process in situ, a yellow light-emitting diode (LED, 589 nm±10 nm) is used to provide trans-illumination through the photoresin; the signals are routed to a charge-coupled device (CCD) camera in the left detection arm via the objective lens, DM, which is turned 90 degrees from the calibration mode, and a relay lens (L7).

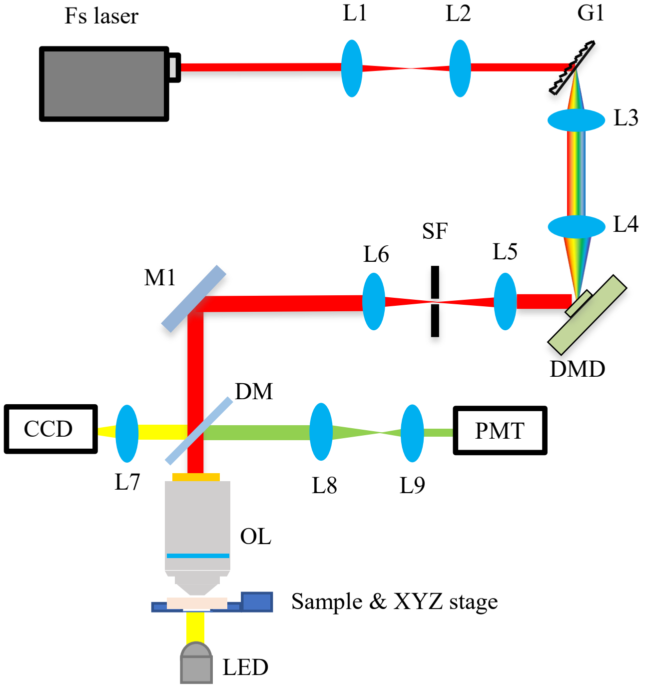

Fig. 1. Optical configuration of the DMD-based TPP fabrication system. L1-L11: convex lenses (f_{L1}, f_{L2}, f_{L3}, f_{L4}, f_{L5}, f_{L6}, f_{L7}, f_{L8}, f_{L9}=50, 50, 100, 250, 200, 200, 100, 100, 25.4 mm, respectively); G1: blazed transmission grating; DMD: digital micromirror device; SP: spatial filter; M1: high-reflectivity mirror; DM: dichroic mirror; CCD: charge-coupled device; PMT: photomultiplier tube.

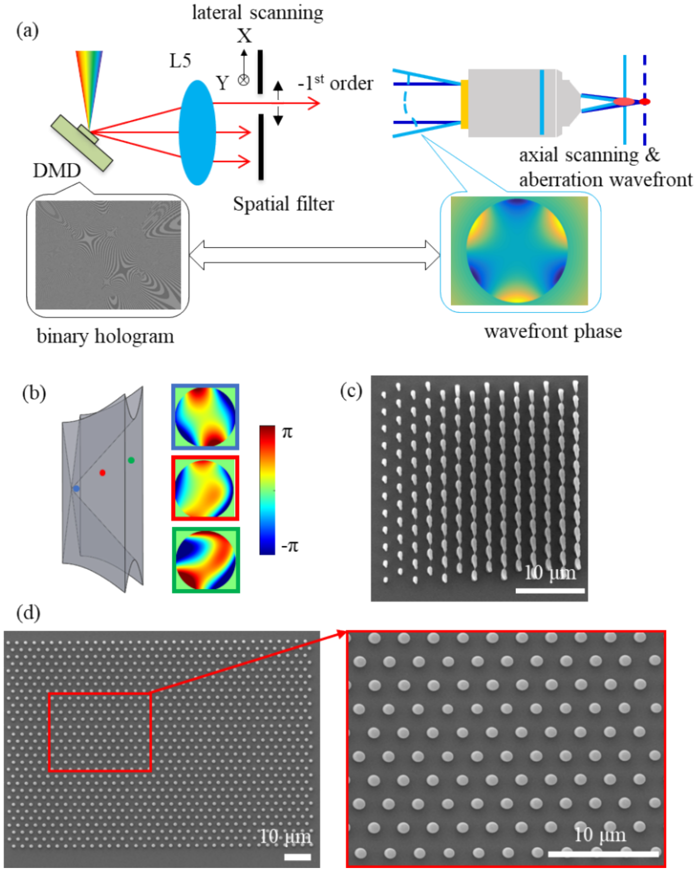

Fig. 2. Aberration-free TPP-printing based on sensorless AO algorithm. (a) Illustration of laser scanning by using the aberration-free −1st order beam, generated by a binary hologram; the hologram is synthesized by superposing the scanning wavefront and distortion-correction wavefront. (b) Distorted wavefront (right) measured at three different locations in the DMD working space (left), i.e., the gray shaded area. (c) & (d) Printed micropillar array without and with AO correction, respectively.

2.3. Theoretical development for binary hologram-based AO correction

To optimize the PSF, which may be intrinsically distorted by the optical system, photoresin, and discrete sampling process during hologram generation, we implement the sensorless AO algorithm to the TPP fabrication platform via the DMD, i.e., the DMD simultaneously serves as a 3D random-access scanner and an adaptive element to compensate the distorted wavefront. This is achieved by superposing the 3D scanning and AO correction wavefronts and converting them to binary holograms. Firstly, Eq. (1) is used to convert an arbitrary wavefront into a binary hologram [20]:

$$h(i,j) = \begin{cases} 1, & -\frac{q}{2} \leq \frac{\phi(x,y)}{2\pi} + n \leq \frac{q}{2} \\ 0, & otherwise \end{cases} \tag{1}$$

where h(i, j) ∈ {0, 1} represents the pixels on a DMD; 1 and 0 refer to the "on" and "off" states, respectively; $\phi(x,\ y)$ represents the phase of an arbitrary wavefront; and q is a constant that determines the width of the fringes, which is set to ½ to maximize the power efficiency in our experiments. Next, let the phase $\phi(x,\ y)$ be the sum of the 3D scanning and distortion wavefronts, which can be mathematically expressed as

$$\phi(x,y) = \frac{2\pi R(x,y)}{T} + \frac{\pi(x^2+y^2)}{\lambda f} + \phi_{distortion}(x,y) \tag{2}$$

where the first term $2\pi R\ (x,\ y)/\ T$ is the tilted phase that controls the lateral position of a laser focus; $R\ (x,\ y) = x \cdot sin(\alpha) + y \cdot cos(\alpha)$; α is the tilt angle of the fringe patterns; T is the grating period of the hologram; the second term $\pi(x^2 + y^2)/\lambda f$ is the spherical wavefront that controls the axial position of a laser focus; λ is the wavelength; f is the effective focal length; and the last term $\phi_{distortion}$ represents a distorted wavefront for AO correction. As such, 3D random-access scanning and AO correction can be achieved simultaneously, as illustrated in Fig. 2(a).

We use Zernike polynomials to model an arbitrarily distorted wavefront [19,21], which is expressed as a linear combination of N Zernike terms in Eq. (3).

$$\phi_{distortion}(x,y) = \sum\nolimits_{j=1}^{N} a_j Z_j + \phi_{error}(x,y) \tag{3}$$

where Z_j is the j^{th} Zernike term and a_j is the coefficient of j^{th} Zernike mode.

As the aberration is not uniform in the DMD work space and can vary significantly based on our experimental observation, localized AO correction is critical to ensure high-resolution and uniform 3D printing. To address the issue, we experimentally measured the wavefront distortion over the entire work space using 100 selected sub-areas with a lateral and axial interval of 20 µm and 10 µm respectively. During the measurement, the right detection arm in the system is used, as shown in Fig. 1, where the PMT collects the fluorescent signals from the photoresist. In each measurement, the first four orders of Zernike modes are used to reconstruct a distorted wavefront, i.e., a total of 11 Zernike terms are used, excluding the terms for tip, tilt, and defocus that are responsible for lateral and axial scanning operations. The average intensity of a measured image, which has an approximate size of 20 × 20 pixels, is used as the evaluation metric, so the optimization problem is to identify a set of coefficients that maximize the quadratic sum of the image intensity, as descried in Eq. (4):

$$A = \arg\max_{A}\left(\sum I(x,y)^2\right) \tag{4}$$

where $A = (a_1,\ a_2,\ \ldots,\ a_N)$ is the vector of Zernike coefficients; and $I(x,\ y)$ is the intensity of a pixel $(x,\ y)$ in the fluorescent image. As the Zernike terms are orthogonal to each other, the optimal coefficient of each Zernike term can be found sequentially. The found coefficients are then updated to the binary hologram; this procedure repeats until all Zernike coefficients are found. To solve the optimization problem in Eq. (4), a combined hill-climbing and bisection algorithm is used. As such, the coefficient of each Zernike mode can be found through the following three steps:

Step 1: Initialize the coefficients, i.e., A = zeros (N, 1), and begin the search from the first term, a_1. Set three temporary values for a_1 as (-a, 0, a), where the interval is a (e.g., $a = 0.4$ is employed in our implementation).

Step 2: Acquire three images with the three temporary A. Calculate the sum of each pixel's intensity square. If the best one is the middle image, change the temporary value of a_1 by keeping the middle value and dividing the interval by 2, i.e., (-a/2, 0, a/2). If the best one is the first or the last image, change the temporary value of a_1 by shifting the three values by subtracting or adding an interval, i.e., (−2a, -a, 0) or (0, a, 2a), respectively. Repeat this step until the interval becomes smaller than the target value, e.g., < 0.03, and set the value of a_1 to the middle one.

Step 3: Proceed to Step 1 for the next term a_2. Repeat Step 1–3 until all N coefficients are determined.

3. Results

In this section, we present the TPP fabrication results to demonstrate the effectiveness of the AO correction and stitch-free printing methods as well as the unique capabilities of the DMD system including discrete power control, random-access scanning, and arbitrary trajectory planning.

3.1. Localized AO correction and fabrication of metamaterials

Figure 2(b) presents the measured wavefronts in the color-labeled boxes at three selected locations (among the 100 sub-areas) in the DMD work space, where one can observe the significant aberration difference in each point. For any unmeasured points in the work space, the Zernike coefficients are obtained by linear interpolation based on the optimal Zernike coefficients from the nearby calibrated sub-areas; typically eight sub-areas are used for interpolation. (Note that the calibration process is fully automated and the interpolation error is negligible when the sub-area distance is set to 20 µm and 10 µm in lateral and axial directions respectively.) Fig. 2(c) and 2(d) present the scanning electron microscope (SEM) images of TPP printed micropillar array with a pillar diameter of 1.2 µm and pitch of 3 µm without and with AO correction, respectively. The results show that without AO correction the shape of micropillars is severely distorted due to the distorted PSF; and with AO correction, one may observe that from the zoom-in view the pillar size becomes highly uniform without any observable fabrication errors.

Next, we optimize the printing parameters, i.e., laser power and exposure time, with AO correction; fabrication experiments of nano-bridge structures have been performed with varying laser power, i.e., 3.5–10.5 mW (measured at the objective lens), and exposure time, i.e., 100 µs and 200 µs. Figure 3(a) plots the measured widths of the nano-bridges over different processing parameters. The results indicate that line widths can be precisely controlled with suitable combination of laser power and exposure time, i.e., laser dose, with AO correction; and a thinnest uniform line can be written with a power and exposure time combination of 4.22 mW and 100 µs respectively, as shown in Fig. 3(b) – 3(e). Figure 3(b) and 3(c) present the top and 45° tilt view of the nano-bridge structure. Figure 3(d) and 3(e) present zoom-in views of the nano-bridge structure, which has a measured width and height of 88 nm and 161 nm respectively. Figure 4 presents more fabrication results with AO correction, including a grating structure with a period of 5 µm (Fig. 4(a)); and a split-ring resonator array with a lattice constant of 2 µm (Fig. 4(b)), which is a metamaterial structure for electromagnetic applications [22]. Note that fine metamaterial structures are usually fabricated by electron-beam lithography, which is slow and expensive and generally limited to 2D structures. These results confirm that high-resolution and highly uniform microstructures can be fabricated with the AO correction method.

3.2. Discrete power control and fabrication of gray-level DOEs

Precise and fast control of laser dose is critical to fabricate fine microstructures. If a laser focus is scanning at a constant speed, i.e., the exposure time is a constant, the laser power then directly determines the dose or voxel size. In our system, the laser intensity of a scanning focus is pre-encoded in a binary hologram via Eq. (5)

$$\phi_p = arg(e^{i\phi} + we^{i\phi_0}) \tag{5}$$

where ϕ_p is the new phase term that carries the intensity information; ϕ is the phase calculated from Eq. (2); ϕ_0 is a constant phase term, where π/6 is used in our experiments; and w is an adjustable weighting factor that determines the laser power distribution between the −1st order beam, which carries the designed wavefront information, and the 0th order beam. Figure 5(a) presents a simulation and experimental study to verify the precise laser intensity control via binary holography, where the normalized −1st beam intensity continuously decreases as w increases from 0 to 2; as the entire system is discrete, the minimal power increment is ~0.01% of the

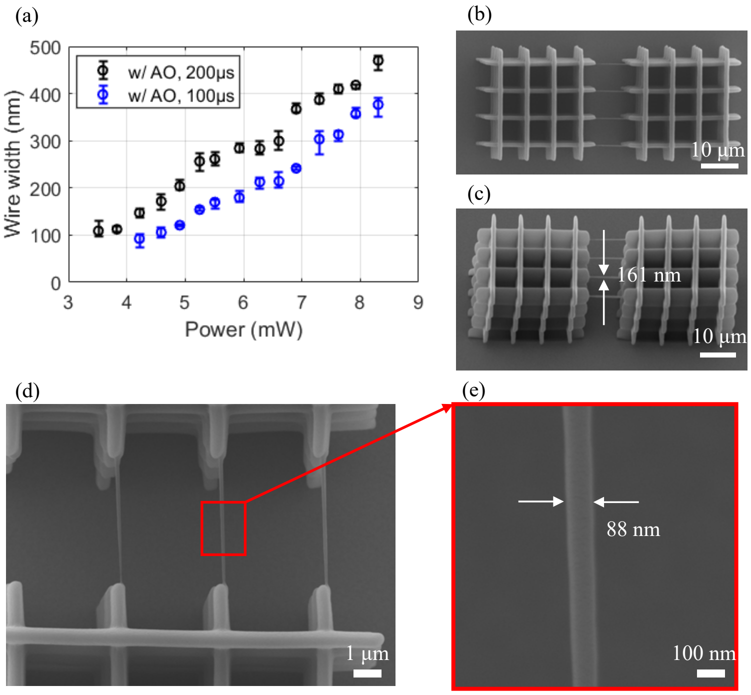

Fig. 3. Calibration of laser dose and line width. (a) Measured widths of suspended nano-bridges fabricated with AO correction, using different combinations of laser power (i.e., 3.5–10.5 mW) and exposure time (i.e., 100 μs and 200 μs). (b) Top view and (c) side view of the nano-bridge structures. (d) Minimum line width is 88 nm. (e), Zoom-in view of (d).

output power or 0.5 μW in our experiments, which is smaller than the power fluctuation of the laser source itself. As the designed holograms is scanned at the DMD pattern rate, i.e., 22.7 kHz, the laser intensity (or voxel size) can be altered at the same speed with high repeatability. (See Fig. 4 for intensity calibration experiments.) Based on the discrete power control method, we fabricated a gray-scale DOE that encodes the “CUHK MAE” pattern via iterative Fourier transform algorithm [23]. The DOE, which has a size of 400×400 μm^2 and a pixel size of 2×2 μm^2, is formed by a single-layer structure fabricated by raster-scanning the laser focus while rapidly altering the laser intensity. (See Visualization 1 for a video demonstration that compares the discrete power control for fabricating the DOEs via raster-scanning and random-access scanning methods.) Fig. 5(b) presents the SEM images of the DOE, where one may observe the microstructures are precisely fabricated with sharp edges and the laser dose induced height (phase) difference is uniform. Figure 5(c) and 5(d) present the DOE encoded pattern and measured results, which again confirms the accuracy of the fabricated DOE. The image in Fig. 5(d) is generated by illuminating the DOE with a 780 nm laser; the diffraction pattern is projected to a white screen and recorded by a CCD camera. (See Visualization 2 for more fast laser dose control demonstrations.)

The power efficiency of the DMD-based TPP fabrication this system is measured to be ~4%, where most energy is lost from the diffraction of DMD [11]. Note that our Ti:sapphire system has an average power of 2.5W, which provides ample power (~100 mW) for TPP fabrication.

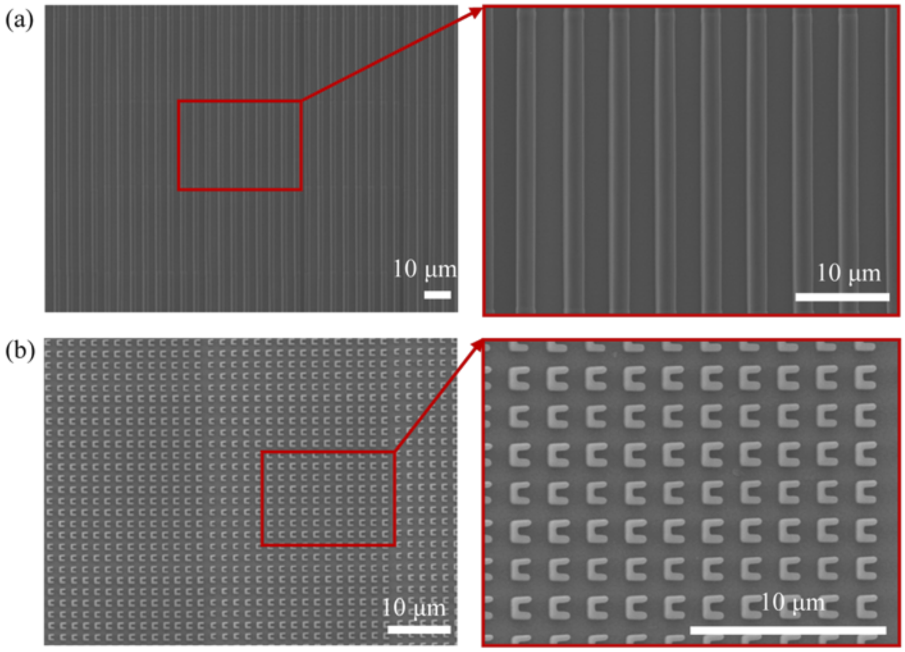

Fig. 4. Fabrication of microstructures with AO correction. (a) Optical grating with a period of 5 µm. (b) Split-ring resonator array with a lattice constant of 2 µm.

3.3. *Stitch-free large area printing*

To achieve high-precision nanofabrication over a large-area, stitching errors must be addressed. Stitching is an unavoidable process for any 3D printing system when the designed structure is larger than the work space of the laser scanning system, i.e., the sample stage is held stationary during printing while the laser scans over the DMD work space, i.e., 103 × 206 × 524 µm^3. After completion, the sample stage moves to the next volume for processing. For photopolymerization-based 3D printing, e.g., TPP, stitching errors are mainly attributed to (1) the volume shrinkage after photopolymerization, which can be clearly observed in Visualization 1 for the random-access scanning case; and (2) positioning errors of the sample stage, which result in geometric errors and non-uniform index distribution in printed structures, e.g., lens or 3D scaffolds, which compromise the quality and performance of the printed structure. Inspired by the infinite field of view (iFOV) concept from Aerotech, we have developed a stitch-free printing process, i.e., the sample stage is continuously moving during the DMD fabrication processes such that the volume to be printed is continuously fed to the laser processing field until the entire structure is completed. To realize this, the DMD and sample stage are synchronized via a PXI controller (National Instruments), where the stage is commanded to move at a constant speed (i.e., 5 - 10 µm/s) while the laser foci are scanning at 22.7 kHz via binary holograms. To compensate the displacement introduced by the moving stage during printing, the coordinates of each laser focus and fabrication trajectory are pre-calculated and converted into binary holograms automatically via a custom-developed program. Notably, for ultra-large structures, the designed holograms are being continuously loaded to the DMD memory for uninterrupted printing. The control flow chart for the stitch-free process is shown in Fig. 6.

Figure 7(a) and 7(b) present a large-area micro-pillar array for photonic applications, fabricated by the stitch-free approach and conventional stitching approach, respectively. Each pillar has a diameter of 1.7 µm; the distance between adjacent pillars are 3.2 µm. In Fig. 7(b), one can

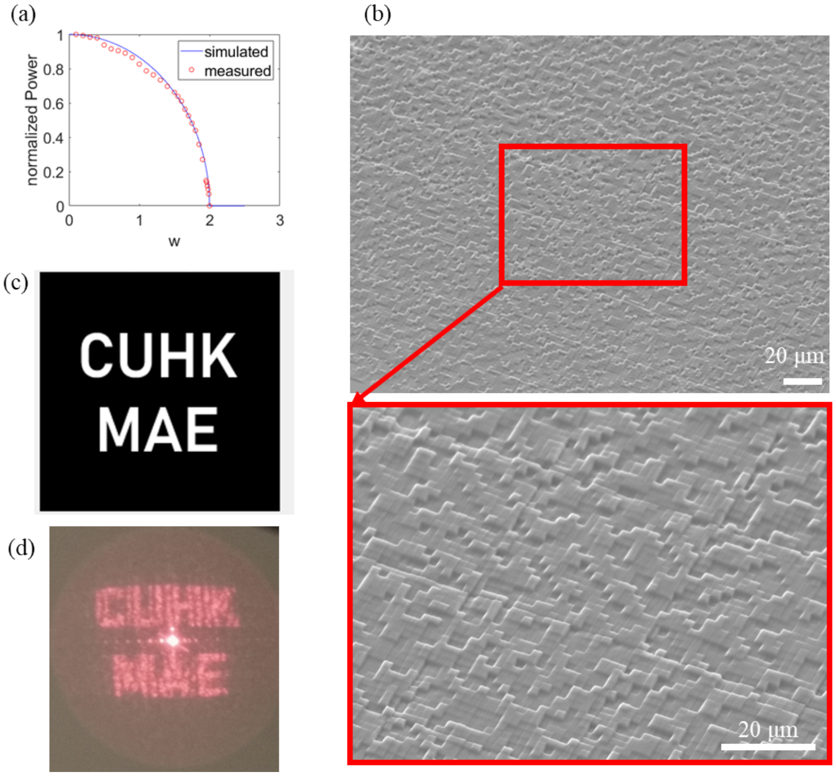

Fig. 5. Fabrication of gray-scale DOE by discrete laser power control. (a) Simulated and measured power of the −1st order beam with w increasing from 0 to 2. (b) SEM image of the printed gray-scale DOE, which encodes the "CUHK MAE" pattern, as shown in (c) & (d) Measured diffraction pattern.

clearly observe the stitching errors among each printed area with a size of 35×26 µm^2 due to sample stage positioning errors. In contrast, in Fig. 7(a) no stitching errors have been observed over the entire array which has a size of 1×1 mm^2. From the zoom-in view, we can confirm the pillar array are precise and uniform. Figure 7(c) and 7(d) present a four-layer large-area woodpile structure for 3D cell culture applications, fabricated by the stitch-free approach and conventional stitching approach, respectively. In Fig. 7(d), a $100 \times 100 \times 14$ µm^3 logpile structure is printed via 3×3 stitches, where stitching errors can be clearly observed, which is expected. In Fig. 7(c), a large-area, i.e., $400 \times 400 \times 14$ µm^3, woodpile structure is continuously printed via the stitch-free approach. From the zoom-in views, we can confirm the woodpile structures are uniform without any visible stitching errors. (See Visualization 3 for a video demonstration of stitch-free continuous fabrication) Based on the stitch-free approach, we further printed large-scale structures for demonstration, including a 500 µm tall Eiffel Tower; arrays of large helical springs; and 3D metamaterial structure, shown in Fig. 8(a) – 8(c) respectively. Notable, the helical springs in Fig. 8(b) is fabricated via scanning the laser focus along the helical trajectory, which cannot be performed via conventional raster-scanning systems. On the other hand, in comparison to previously demonstrated stitch-free systems [24], which combined a pair of galvanometric scanners with a linear stage, the DMD-scanner achieves better precision (~200 nm) owing to its inertia-free scanning characteristics.

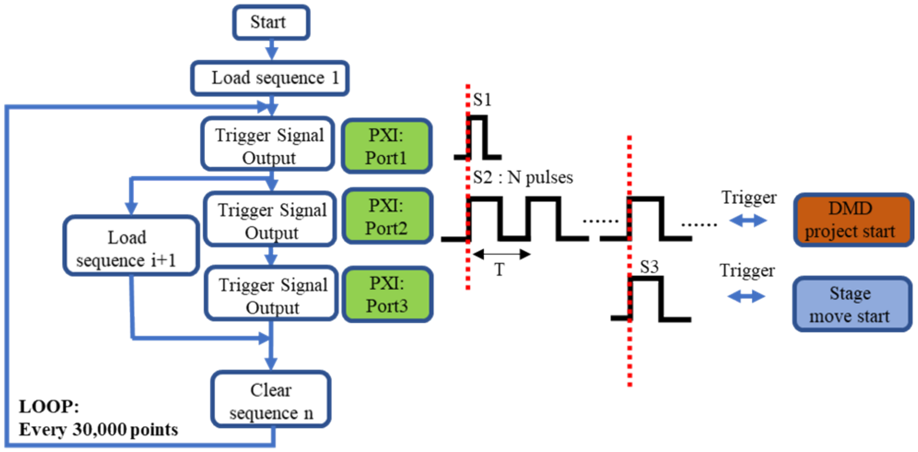

Fig. 6. Flow chart of controlling stitch-free large area printing. To synchronize the motion between the DMD scanner and the translational stage and to ensure continuous fabrication with a limited DMD memory, the DMD memory is divided into two parts, one for displaying the loaded holograms, and the other for loading the next scanning hologram sequence. After the first hologram sequence (i.e., 30,000 holograms) is loaded, PXI Port1 sends out a pulse signal to initiate the printing process. In parallel, PXI Port2 and Port3 send out pulse sequences to respectively control the DMD and translational stage, which are operated in the trigger mode. This process repeats until the completion of fabrication. Each sequence contains 30,000 binary holograms.

3.4. Arbitrary trajectory and microlens printing

In this section, we demonstrate the use of 3D random-access scanning for fabricating microlenses with different printing trajectories to achieve improved lens surface quality, optical performance, and reduced fabrication time. In the DMD scanner, each laser focus in space is represented by a unique binary hologram, and moving the laser focus is achieved by sequentially displaying the different holograms on the DMD. Notably, each hologram also includes a pre-encoded laser power. As such, trajectory planning and gray-scale control can be simply realized by altering the hologram displaying sequence; and the total fabrication time is only determined by the number of holograms regardless the scanning sequence. Although path planning via multi-axis positioners is a well-known approach to improve the printing results in the field of additive manufacturing [25,26], it has rarely been applied in TPP fabrication due to the limited scanning capability of galvo-scanners or other inertia-based scanners. Here, we apply the DMD-scanner to demonstrate (1) multi-zone printing and (2) flood-filling printing; and compare the fabrication results with the conventional layer-by-layer printing approach. Note that the flood-filling printing approach is also called conformal printing in the computer-aided design (CAD) and graphics community [26,27].

Figure 9 present the microlens fabrication results, where Fig. 9(a) – 9(c) illustrate the three scanning approaches, i.e., layer-by-layer printing, dual-zone printing, and flood-filling printing, respectively; Fig. 9(d) – 9(f) present the SEM images of the corresponding printed microlenses; and Fig. 9(g) – 9(i) present the optical characterization results. Each microlens has a diameter and focal length of 35.0 µm and 37.5 µm respectively. In the experiments, the writing laser power is mostly held constant at 7.5 mW (measured under the objective lens); except for the dual-zone printing case that the inner zone is fabricated with a power of 11.0 mW to improve fabrication time, i.e., the point distance in the inner region is two times larger and thus the fabrication (scanning) time is reduced by 50%. The exposure time is held constant for all points at 44 µs, i.e., scanning rate is 22.7 kHz. The total print time for Fig. 9(d) – 9(f) are 12, 7, 12

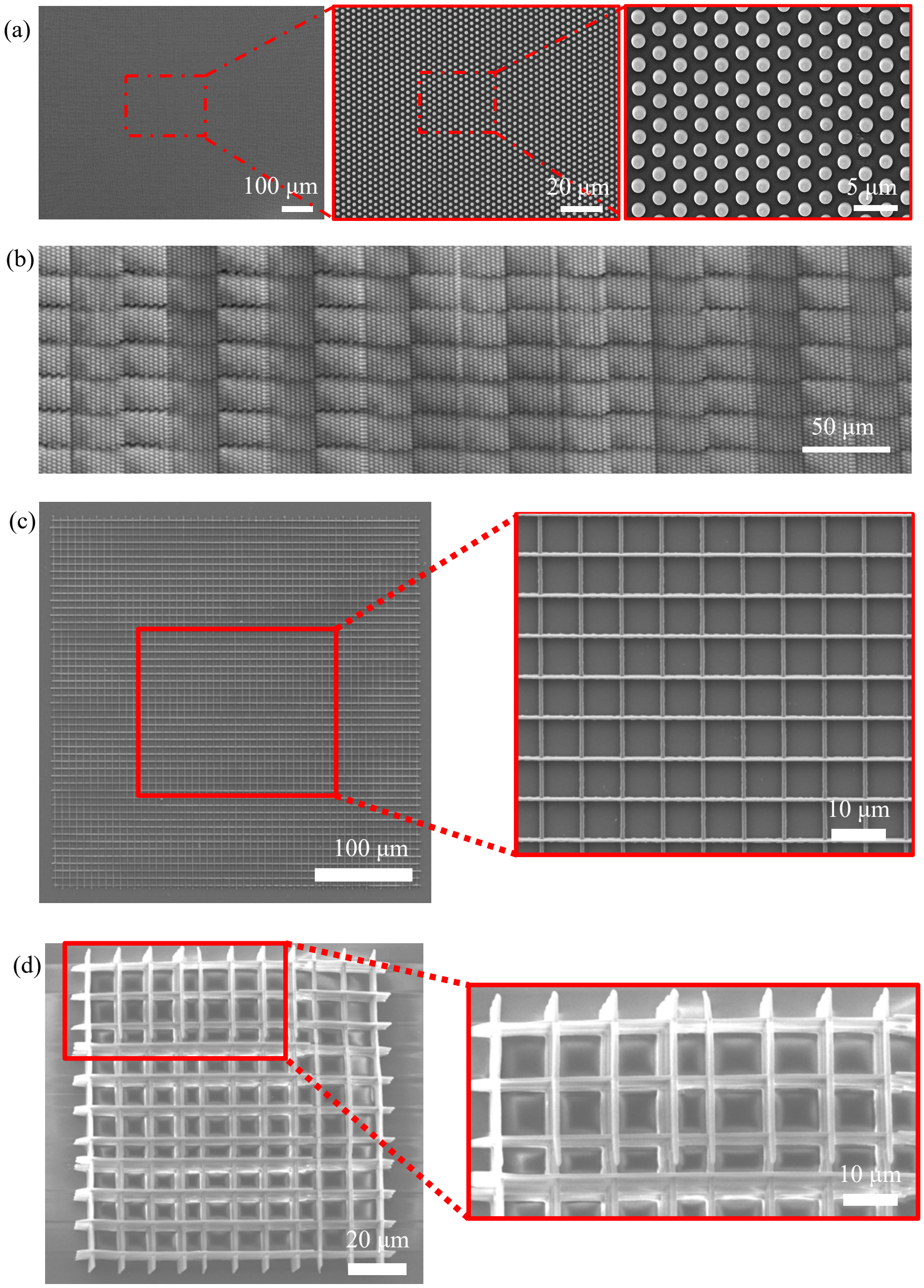

Fig. 7. Stitch-free fabrication of large-area metamaterial structures. (a) & (b) SEM images of a large-area micropillar array fabricated via the stitch-free method and conventional method, respectively. (c) & (d) SEM images of a large woodpile structure fabricated via the stitch-free method and conventional method, respectively. Micropillar array fabricated via the conventional stitching method, where lateral and axial stage positioning errors can be observed.

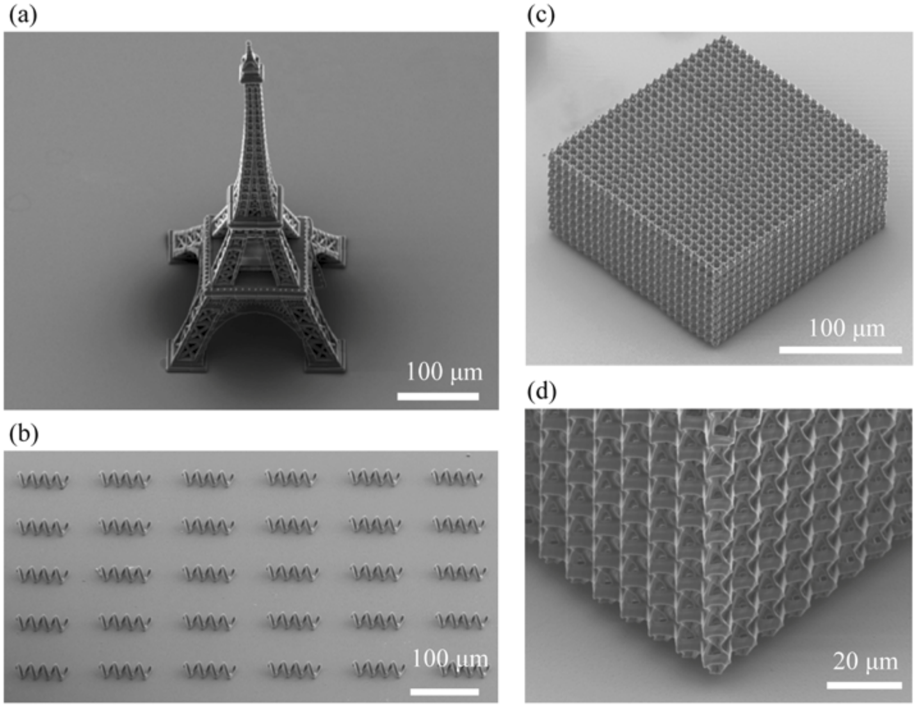

Fig. 8. Examples of large-scale 3D structures. (a) TPP-printed Eiffel Tower with a size of ~$240 \times 240 \times 500$ μm^3. (b) Arrays of helical springs. (c) TPP-printed 3D metamaterial structure; and (d) Zoom-in view of (c).

seconds respectively, i.e., altering the scanning sequence does not change the fabrication time. From the SEM images, one may observe clear stair-case fabrication errors in Fig. 9(d), which is expected; these errors are largely eliminated in Fig. 9(e) and 9(f), where the lens surfaces are greatly smoothened by the different scanning strategies. From Fig. 9(g) – 9(i), the full width half maximum (FWHM) of each microlens is measured to be 1.08 μm, 0.94 μm and 0.93 μm, respectively. (The theoretical FWHM is calculated to be 0.88 μm.) These results confirm our observation in Fig. 9(d) – 9(f) and indicate that the flood-filling algorithm can effectively improve the surface quality and performance of microlenses or other optical components that require smooth surfaces. It is worth to note that further optimization of the optical surface may be achieved by gray-scale printing of the lens shell in Fig. 9(d) or 9(e).

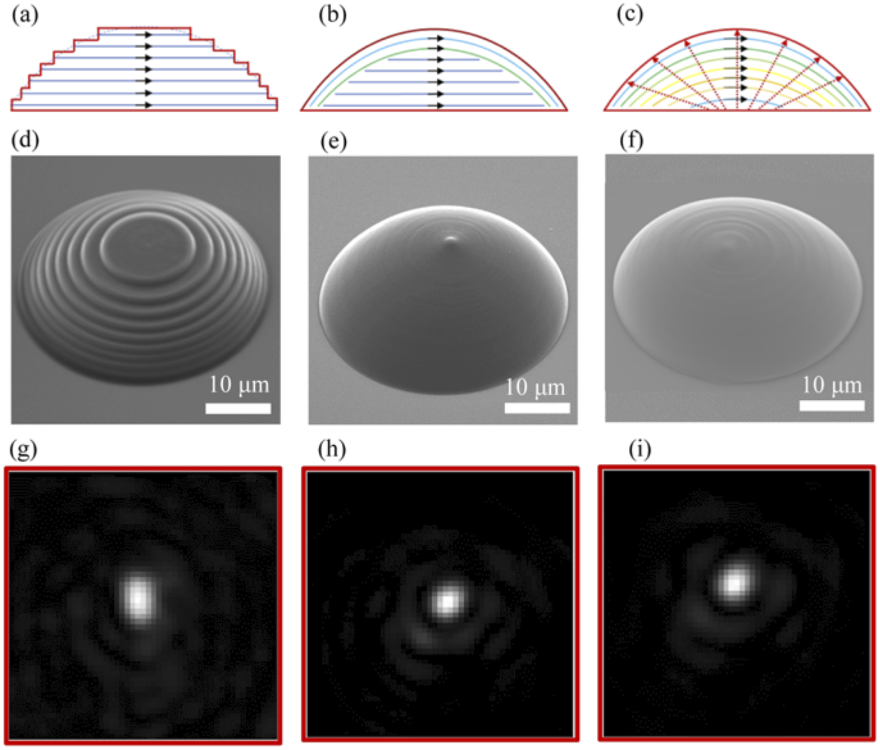

Fig. 9. Fabrication of microlenses via different scanning trajectories. (a) Planar layer-by-layer printing with equal axial step distance. (b) Dual-zone printing, where the interior is printed via the standard layer-by-layer approach with high laser power and the outer shell is printed separately with low power. (c) Flood-filling printing, where curved shells are printed from the center to the outer lens surface. (d) – (f) SEM images of the printed microlenses in (a) – (c) respectively. (g) – (i) Measured focal points of microlenses (d) – (f) respectively.

4. Conclusion

We have introduced a DMD-based TPP fabrication system that realizes aberration-free large-area 3D printing with a resolution of 88 nm and 161 nm in the lateral and axial direction respectively. Specifically, aberration of each point in the DMD work space is fully corrected by a unique distortion correction phase modeled by the Zernike polynomial using a DMD, which simultaneously performs 3D scanning and wavefront correction. Large-area stitch-free writing is realized by effectively synchronizing the DMD and the sample positioner to achieve continuous fabrication. As the DMD is an inertia-free scanner, the overall precision of the stitch-free writing method is limited by the precision of the sample positioner. Fast and precise laser dose control is realized by the discrete power control based on binary holography. These new capabilities are demonstrated and characterized by the fabrication of gray-scale DOEs, metamaterial structures, e.g., micropillar, split-ring arrays and woodpile structures. Lastly, various scanning strategies have been adopted to fabricate microlenses with improved surface quality and optical performance, demonstrating the effectiveness of random-access scanning capability of the DMD fabrication system, which will be an attractive solution for printing micro- and nanostructures with improved resolution, rate, and yield.

Funding. Research Grants Council (14203020); Innovation and Technology Fund (ITS/178/20FP); Centre for Perceptual and Interactive Intelligence under the Innovation and Technology Fund.

Disclosures. The authors declare no conflicts of interest.

Data availability. Data underlying the results presented in this paper are not publicly available at this time but may be obtained from the authors upon reasonable request.

References

1. S. Maruo, O. Nakamura, and S. Kawata, "Three-dimensional microfabrication with two-photon-absorbed photopolymerization," Opt. Lett. **22**(2), 132–134 (1997).
2. S. Kawata, H.-B. Sun, T. Tanaka, and K. Takada, "Finer features for functional microdevices," Nature **412**(6848), 697–698 (2001).
3. A. K. Nguyen and R. J. Narayan, "Two-photon polymerization for biological applications," Mater. Today **20**(6), 314–322 (2017).
4. W. Lin, D. Chen, and S. Chen, "Emerging Micro-additive Manufacturing Technologies Enabled by Novel Optical Methods," Photonics Res. **8**(12), 1827–1842 (2020).
5. M. Rumi and J. W. Perry, "Two-photon absorption: an overview of measurements and principles," Adv. Opt. Photonics **2**(4), 451–518 (2010).
6. M. T. Raimondi, S. M. Eaton, M. M. Nava, M. Laganà, G. Cerullo, and R. Osellame, "Two-photon laser polymerization: from fundamentals to biomedical application in tissue engineering and regenerative medicine," J. Appl. Biomater. Funct. Mater. **10**(1), 56–66 (2012).
7. H. B. Sun, K. Takada, M. S. Kim, K. S. Lee, and S. Kawata, "Scaling laws of voxels in two-photon photopolymerization nanofabrication," Appl. Phys. Lett. **83**(6), 1104–1106 (2003).
8. X. Zhou, Y. Hou, and J. Lin, "A review on the processing accuracy of two-photon polymerization," AIP Adv. **5**(3), 030701 (2015).
9. T. W. Lim, S. H. Park, and D. Y. Yang, "Contour offset algorithm for precise patterning in two-photon polymerization," Microelectron. Eng. **77**(3-4), 382–388 (2005).
10. H. B. Sun and S. Kawata, "Two-photon laser precision microfabrication and its applications to micro-nano devices and systems," J. Lightwave Technol. **21**(3), 624–633 (2003).
11. Q. Geng, C. Gu, J. Cheng, and S. C. Chen, "Digital micromirror device-based two-photon microscopy for three-dimensional and random-access imaging," Optica **4**(6), 674–677 (2017).
12. Q. Geng, D. Wang, P. Chen, and S. Chen, "Ultrafast Multi-focus 3-D Nano-fabrication based on Two-photon Polymerization," Nat. Commun. **10**(1), 2179 (2019).
13. S. K. Saha, D. Wang, V. H. Nguyen, Y. Chang, J. S. Oakdale, and S. Chen, "Scalable Submicrometer Additive Manufacturing," Science **366**(6461), 105–109 (2019).
14. M. Emons, K. Obata, T. Binhammer, A. Ovsianikov, B. N. Chichkov, and U. Morgner, "Two-photon polymerization technique with sub-50 nm resolution by sub-10 fs laser pulses," Opt. Mater. Express **2**(7), 942–947 (2012).
15. Z. Gan, Y. Cao, R. A. Evans, and M. Gu, "Three-dimensional deep sub-diffraction optical beam lithography with 9 nm feature size," Nat. Commun. **4**(1), 2061 (2013).
16. P. S. Salter and M. J. Booth, "Adaptive optics in laser processing," Light: Sci. Appl. **8**(1), 110 (2019).
17. N. Ji, "Adaptive optical fluorescence microscopy," Nat. Methods **14**(4), 374–380 (2017).
18. M. J. Booth, "Adaptive optical microscopy: the ongoing quest for a perfect image," Light: Sci. Appl. **3**(4), e165 (2014).
19. M. Ren, J. Chen, D. Chen, and S. C. Chen, "Aberration-free 3D imaging via DMD-based two-photon microscopy and sensorless adaptive optics," Opt. Lett. **45**(9), 2656–2659 (2020).
20. W. H. Lee, "Binary synthetic holograms," Appl. Opt. **13**(7), 1677–1682 (1974).
21. R. J. Noll, "Zernike polynomials and atmospheric turbulence," J. Opt. Soc. Am. **66**(3), 207–211 (1976).
22. S. Linden, F. B. P. Niesler, J. Förstner, Y. Grynko, T. Meier, and M. Wegener, "Collective effects in second-harmonic generation from split-ring-resonator arrays," Phys. Rev. Lett. **109**(1), 015502 (2012).
23. F. Wyrowski and O. Bryngdahl, "Iterative Fourier-transform algorithm applied to computer holography," J. Opt. Soc. Am. A **5**(7), 1058–1065 (1988).
24. L. Jonušauskas, D. Gailevičius, S. Rekštytė, T. Baldacchini, S. Juodkazis, and M. Malinauskas, "Mesoscale laser 3D printing," Opt. Express **27**(11), 15205–15221 (2019).
25. J. Jiang and Y. Ma, "Path planning strategies to optimize accuracy, quality, build time and material use in additive manufacturing: a review," Micromachines **11**(7), 633 (2020).
26. C. Dai, C. C. L. Wang, C. Wu, S. Lefebvre, G. Fang, and Y. Liu, "Support-free volume printing by multi-axis motion," ACM Trans. Graph. **37**(4), 1–14 (2018).
27. G. Fang, T. Zhang, S. Zhong, X. Chen, Z. Zhong, and C. C. L. Wang, "Reinforced FDM: Multi-axis filament alignment with controlled anisotropic strength," ACM Trans. Graph. **39**(6), 1–15 (2020).